CORE
Metadata, citation and similar papers at core.ac.uk
Provided by Caltech Authors - Main

ACS NANO
Caltech Library
Subscriber access provided by Caltech Library

Article

Hot Hole versus Hot Electron Transport at Copper/GaN Heterojunction Interfaces

Giulia Tagliabue, Joseph S DuChene, Adela Habib, Ravishankar Sundararaman, and Harry A Atwater

ACS Nano, **Just Accepted Manuscript** • DOI: 10.1021/acsnano.0c00713 • Publication Date (Web): 14 Apr 2020

Downloaded from pubs.acs.org on April 14, 2020

Just Accepted

"Just Accepted" manuscripts have been peer-reviewed and accepted for publication. They are posted online prior to technical editing, formatting for publication and author proofing. The American Chemical Society provides "Just Accepted" as a service to the research community to expedite the dissemination of scientific material as soon as possible after acceptance. "Just Accepted" manuscripts appear in full in PDF format accompanied by an HTML abstract. "Just Accepted" manuscripts have been fully peer reviewed, but should not be considered the official version of record. They are citable by the Digital Object Identifier (DOI®). "Just Accepted" is an optional service offered to authors. Therefore, the "Just Accepted" Web site may not include all articles that will be published in the journal. After a manuscript is technically edited and formatted, it will be removed from the "Just Accepted" Web site and published as an ASAP article. Note that technical editing may introduce minor changes to the manuscript text and/or graphics which could affect content, and all legal disclaimers and ethical guidelines that apply to the journal pertain. ACS cannot be held responsible for errors or consequences arising from the use of information contained in these "Just Accepted" manuscripts.

is published by the American Chemical Society. 1155 Sixteenth Street N.W., Washington, DC 20036
Published by American Chemical Society. Copyright © American Chemical Society. However, no copyright claim is made to original U.S. Government works, or works produced by employees of any Commonwealth realm Crown government in the course of their duties.

1
2
3
4
5
6
7
8
9
10
11
12
13
14
15
16
17
18
19
20
21
22
23
24
25
26
27
28
29
30
31
32
33
34
35
36
37
38
39
40
41
42
43
44
45
46
47
48
49
50
51
52
53
54
55
56
57
58
59
60

Hot Hole *versus* Hot Electron Transport at Cu/GaN Heterojunction Interfaces

Giulia Tagliabue[1,2], Joseph S. DuChene[1], Adela Habib[3], Ravishankar Sundararaman[3] and Harry A. Atwater[1,*]

[1]Thomas J. Watson Laboratory of Applied Physics and Joint Center for Artificial Photosynthesis, California Institute of Technology, Pasadena, California 91125 United States.

[2]Laboratory of Nanoscience for Energy Technologies (LNET), EPFL, 1015 Lausanne, Switzerland

[3] Department of Materials Science and Engineering, Rensselaer Polytechnic Institute, 110 8th Street, Troy, New York 12180, United States.

*haa.caltech.edu

Abstract

Among all plasmonic metals, copper (Cu) has the greatest potential for realizing optoelectronic and photochemical hot-carrier devices, thanks to its CMOS compatibility and outstanding catalytic properties. Yet, relative to gold (Au) or silver (Ag), Cu has rarely been studied and the fundamental properties of its photoexcited hot carriers are not well understood. Here, we demonstrate that Cu nanoantennas on *p*-type gallium nitride (*p*-GaN) enables hot-hole-driven photodetection across the visible spectrum. Importantly, we combine experimental measurements of the internal quantum efficiency (IQE) with *ab initio* theoretical modelling to clarify the competing roles of hot-carrier energy and mean-free path on the performance of hot-hole devices above and below the interband threshold of the metal. We also examine Cu-based plasmonic photodetectors on corresponding *n*-type GaN substrates that operate *via* the collection of hot electrons. By comparing hot hole and hot-electron photodetectors that employ the same metal/semiconductor interface (Cu/GaN), we further elucidate the relative advantages and limitations of these complementary plasmonic systems. In particular, we find that harnessing hot holes with *p*-type semiconductors is a promising strategy for plasmon-driven photodetection across the visible and ultra-violet regimes. Given the technological relevance of Cu and the fundamental insights provided by our combined experimental and theoretical approach, we anticipate that our studies will have a broad impact on the design of hot-carrier optoelectronic devices and plasmon-driven photocatalytic systems.

Keywords: plasmonics, hot carriers, photodetection, hot holes, *p*-type GaN, copper

1
2
3
4
5
6
7
8
9
10
11
12
13
14
15
16
17
18
19
20
21
22
23
24
25
26
27
28
29
30
31
32
33
34
35
36
37
38
39
40
41
42
43
44
45
46
47
48
49
50
51
52
53
54
55
56
57
58
59
60

Noble metal nanostructures support surface plasmons across a wide spectral window spanning the ultraviolet to near-infrared regions of the electromagnetic spectrum. This strong light-matter interaction enables plasmonic-metal nanostructures to serve as optical nanoantennas capable of efficiently harvesting incident photons.[1] These nanoantennas are often composed of metals such as Au,[2,3] Ag,[4,5] and more recently Al,[6] while Cu has received relatively little attention.[7,8] This deficiency of Cu-based systems is largely related to chemical instabilities arising from surface oxidation processes that eventually render the plasmonic metal into an oxide (*i.e.* Cu_2O or CuO) under ambient conditions. Despite these challenges, there are several potential advantages associated with using metallic Cu for the plasmonic element in a device architecture. As an earth-abundant metal that is fully CMOS-compatible, Cu-based nanoantennas could facilitate widespread implementation of plasmonic components into a broad array of optoelectronic devices.[9] Cu also exhibits catalytic activity for a variety of chemical reactions,[10,11] offering numerous opportunities for plasmon-driven photochemistry. This auspicious combination of tunable optoelectronic properties coupled with diverse catalytic behavior suggests that Cu nanostructures have the potential to broadly impact advancements in photodetection and photocatalysis. To fulfill these promises, however, requires an improved understanding of the fundamental properties of photo-excited hot carriers in Cu nanostructures.

Optical excitation of metallic nanostructures, either *via* plasmon-assisted indirect transitions (*sp*-band to *sp*-band) or direct interband transitions (*d*-band to *sp*-band), generates highly-energetic "hot" carriers above (electrons) and below (holes) the metal Fermi level (E_F)[12] (Figure 1a). Prompt collection of these hot carriers from the metal can be used to either generate a photocurrent *via* injection into an adjacent semiconductor or drive a chemical reaction *via* injection into a molecular orbital of an adsorbate.[13–16] To overcome the fast relaxation rates of hot carriers in the metal, charge separation is typically accomplished by ultrafast charge injection across an interfacial Schottky barrier (Φ_B) established at a metal/semiconductor heterojunction[3,17] (Figure 1b). However, only those carriers that reach the metal/semiconductor interface with the appropriate momentum (k) and energy (E) can surmount the Schottky barrier.[18,19] Therefore, the energy-dependent mean-free path (l_{mfp}) of photo-excited hot carriers, along with their initial energy and momentum distributions, are all important parameters that govern the overall efficiency of plasmonic hot-carrier devices.[12]

1
2
3
4
5
6
7
8
9
10
11
12
13
14
15
16
17
18
19
20
21
22
23
24
25
26
27
28
29
30
31
32
33
34
35
36
37

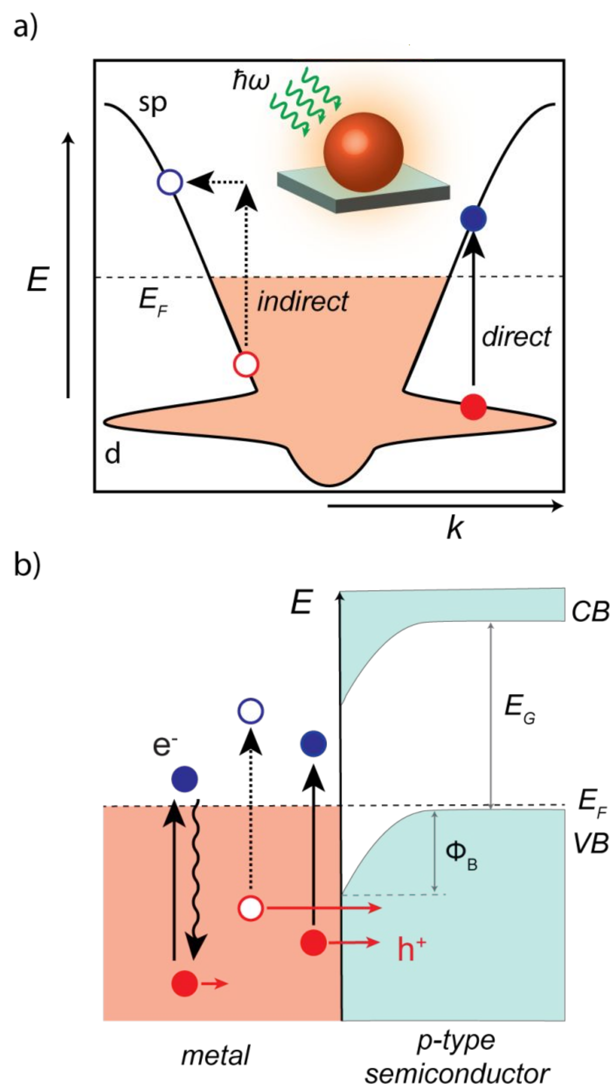

38 **Figure 1: Optical Generation and Collection of Hot Holes in Metals. a)** Hot carriers can be generated in a metal
39
40 through either indirect, intraband transitions between *sp*-band levels involving a phonon (empty circles) or
41
42 through direct, interband transitions from the *d*-band up to the *sp*-band (solid circles). **b)** Qualitative band-
43 alignment diagram at a metal/*p*-type semiconductor heterojunction, denoting the conduction band (CB), valence
44
45 band (VB), and band gap (E_G) of the semiconductor along with the Fermi level (E_F) of the overall system. Hot holes
46
47 generated in the metal differ in their energy as well as their mean-free path. In particular, hot holes from interband
48 transitions (*d*-band to *sp*-band) have higher energies and shorter mean-free paths than hot holes generated via
49
50 intraband (*sp*-band to *sp*-band) transitions. These two properties determine the overall probability of the hot hole
51
52 reaching the metal/semiconductor interface and then being injected over the Schottky barrier (Φ_B) to eventually
53 be collected by the *p*-type semiconductor.
54
55
56
57
58
59
60

Ab initio theoretical calculations indicate that in *d*-band metals, like Au and Cu, photo-excitation above the interband threshold generates a favorable distribution of high-energy hot holes with a peak in probability close to that of the incident photon energy.[12] This feature of hot-hole energy distributions is in stark contrast to that of hot electrons, in which interband transitions yield a distribution that remains highly localized near the metal Fermi level.[12,20,21] It is therefore anticipated that hot-hole generation *via* interband transitions will offer substantial improvements in the generation of highly-energetic hot carriers at visible frequencies where the production of high-energy hot electrons begins to taper off.[20] While promising, it is often argued that the short mean-free path of *d*-band holes substantially restricts their mobility and thereby limits their collection efficiency across an interface (Figure 1). Despite their expected low velocities and short lifetimes,[12] it has been demonstrated that hot holes can be collected from the *d*-bands of Au and Cu nanoparticles *via* injection into the valence band of *p*-type semiconductors.[22–24] Interestingly for the case of Cu nanostructures, it has recently been shown that *d*-band holes close to the band edge exhibit relatively-long lifetimes that can even exceed those of *sp*-band electrons.[8,25] Thus, hot-hole devices composed of Cu nanostructures could present significant advantages for efficient photodetection in the visible regime. To date, however, only a few hot-hole-driven photodetectors have been reported.[17-22] These devices primarily employ semiconductors with relatively small bandgaps (*e.g.* Si), limiting their operation to the near-infrared regime where photo-excitation of hot holes originates from the *sp*-band of the metal.[26–31] Plasmonic photodetectors capable of functioning throughout the visible spectrum *via* collection of hot holes from the metal *d*-bands have yet to be demonstrated. Moreover, the non-parabolic nature of the *d*-bands limits the applicability of simple injection models,[32] such as Fowler theory,[18,19] for modeling the collection of hot holes across a metal/semiconductor heterojunction. Indeed, an appropriate model for hot-hole injection above the interband threshold of the plasmonic metal remains elusive due to the failure of the parabolic-band approximation to properly describe hot holes in the metal *d*-bands.[32] As a result, very little is known about the fundamental processes governing the transport and collection of hot holes from metal nanostructures. Experimentally quantifying the internal quantum efficiency (IQE) of hot-hole injection across a metal/semiconductor interface is therefore critical to clarify the potential opportunities and technological limitations of hot-hole devices.

1
2
3
4
5
6
7
8
9
10
11
12
13
14
15
16
17
18
19
20
21
22
23
24
25
26
27
28
29
30
31
32
33
34
35
36
37
38
39
40
41
42
43
44
45
46
47
48
49
50
51
52
53
54
55
56
57
58
59
60

Here, we study solid-state plasmonic Schottky photodiodes composed of Cu nanoantennas on *p*-type GaN (*p*-GaN) substrates that operate *via* the collection of hot holes across the entire visible regime ($\hbar\omega$ = 1.6 – 2.8 eV). This spectral range spans both the intra- and interband regimes of Cu, allowing careful study of how the incident photon energy and the metal band structure govern the initial generation and subsequent collection of hot holes across the metal/semiconductor interface. Combining the experimentally determined internal quantum efficiency (IQE) of hot-hole-driven photodetection with *ab initio* theoretical modeling of hot-hole generation, transport, and injection across the Cu/*p*-GaN interface reveals the competing effects of hot hole energy and mean-free path in determining the operating efficiency of plasmonic devices. We also examine Cu-based plasmonic photodetectors on corresponding *n*-type GaN substrates that operate *via* hot-electron injection. This complementary system provides a more general understanding of how the subtle interplay between hot-carrier energy and mean-free path impacts the IQE of hot-carrier devices across the visible spectrum. These combined studies reveal that the IQE of hot-electron devices decreases upon exceeding the interband threshold of the metal, while that of hot-hole devices eventually increases as the favorable energy distribution of *d*-band holes ultimately overcomes the reduced mean-free path. Taken together, our results provide general guidelines for the construction of hot-carrier devices with improved collection efficiency and will help expand the use of hot-hole-driven devices for photodetection and plasmon-driven photocatalysis.

1
2
3
4
5
6
7
8
9
10
11
12
13
14
15
16
17
18
19
20
21
22
23
24
25
26
27
28
29
30
31
32
33
34
35
36
37
38
39
40
41
42
43
44
45
46
47
48
49
50
51
52
53
54
55
56
57
58
59
60

Results and Discussion

Realization of plasmonic photodetectors that operate across the visible regime *via* hot-hole injection requires a wide bandgap *p*-type semiconductor support to ensure that any observed photoresponse originates solely from absorption in the metal nanoantenna.[33] In addition, effective charge separation at the metal/semiconductor interface requires the formation of a sizable Schottky-barrier (Φ_B) and hence proper band-alignment between the two materials.[3] Our experimental platform consists of an array of ultrathin (t = 20 – 30 nm) Cu nanoantennas (Figure 2a) fabricated on top of a *p*-type (Mg-doped) GaN epi-film (4 ± 1 µm thick) on a sapphire substrate (see Methods and Supporting Information Figure S1). We use *p*-GaN as the semiconductor support due to its large optical band gap (E_G ~3.4 eV),[22] which excludes visible-light absorption within *p*-GaN and allows for unambiguously assigning the responsivity of the Cu/*p*-GaN device to hot-hole injection from the Cu nanoantennas. The *p*-GaN substrate permits hot-hole conduction while also possessing favorable band alignment[33] relative to the Cu Fermi level that enables the formation of an interfacial Schottky barrier across the Cu/*p*-GaN heterojunction. As an added benefit, we are also able to obtain *n*-type GaN (*n*-GaN) for complementary studies of plasmon-driven hot-electron collection, providing an ideal experimental platform for studying the effects of both hot holes and hot electrons from the same metal with the same semiconductor. The nanoantennas were fabricated from Cu because it supports surface plasmon excitations across a broad spectral range while also being CMOS-compatible with on-chip optoelectronics. The metal thickness was chosen to minimize the transport distance for hot holes from the metal without sacrificing the overall absorption of incident light within the nanoantenna.[33] No interfacial adhesion layer was used to construct the Cu/*p*-GaN heterojunction, excluding parasitic optical absorption from transition-metal adhesion layers (*i.e*. Ti or Cr) commonly used at the metal/semiconductor interface. The presence of an interfacial Schottky barrier (Φ_B ~1.6 eV) at the Cu/*p*-GaN heterojunction was confirmed by photoresponsivity measurements (see Supporting Information Figure S2). An Ohmic contact to *p*-GaN was achieved through deposition of a Ni/Au alloy as previously described,[22] which completes the plasmonic Schottky photodiode by enabling photocurrent collection *via* two micro-contact probes during illumination of the device (see Methods).

As recently demonstrated,[33] analysis of the experimental internal quantum efficiency (IQE) spectrum of a plasmonic photodetector can provide deeper insight into the mechanisms controlling the

1
2
3
4
5
6
7
8
9
10
11
12
13
14
15
16
17
18
19
20
21
22
23
24
25
26
27
28
29
30
31
32
33
34
35
36
37
38
39
40
41
42
43
44
45
46
47
48
49
50
51
52
53
54
55
56
57
58
59
60

generation, transport, and injection of hot carriers across the metal/semiconductor interface. We thus performed IQE measurements on our Cu/*p*-GaN photodiodes to understand the performance of the device as a function of the incident wavelength (λ) or photon energy ($\hbar\omega$). To obtain the IQE($\hbar\omega$) spectrum, we first perform accurate measurements of the absorption spectrum $A(\lambda)$ and external quantum efficiency EQE($\hbar\omega$) spectrum (Figure 2b) of the device using a custom-built experimental setup (see Methods). Fabry-Perot interferences in the high-refractive index GaN epi-layer give rise to the observed fringes in the spectra shown in Figure 2. The surface plasmon resonance of the Cu nanoantennas appears as a broad absorption peak around 800 nm (Figure 2b, grey curve). This spectral assignment is verified by comparison with unpatterned Cu films, which lack any absorption feature at longer wavelengths (Supporting Information Figure S1). Alternatively, the increased absorption for wavelengths shorter than 600 nm ($\hbar\omega \geq 2$ eV) is associated with interband transitions in the Cu film (Figure 2b, grey curve and Figure S1). The EQE($\hbar\omega$) spectrum of the device (Figure 2b, red curve) is obtained by performing wavelength-dependent photocurrent measurements under monochromatic illumination with polarization perpendicular to the nanoantenna (see Methods). First, we record photocurrent maps from the Cu/*p*-GaN device at a particular wavelength to verify the spatial uniformity of the nanoantenna structure (Supporting Information Figure S2). Next, we measure the photocurrent spectrum at several positions within the nanoantenna array to obtain the EQE($\hbar\omega$) of the hot-hole device (Figure 2b, red curve). The EQE($\hbar\omega$) of the Cu/*p*-GaN photodiode increases throughout the entire visible spectrum, but rises much more rapidly beyond 2.4 eV. As a control experiment, no photocurrent was obtained from the bare *p*-GaN substrate in the absence of Cu nanoantennas (Supporting Information Figure S2). We therefore attribute the entire EQE($\hbar\omega$) spectrum observed from the Cu/*p*-GaN photodiode to the injection of hot holes from the Cu nanoantenna into the *p*-GaN support. The IQE($\hbar\omega$) spectrum of the Cu/*p*-GaN device is then obtained by normalizing the EQE($\hbar\omega$) by the absorption spectrum (see Methods). As shown in Figure 2c (solid red curve), the IQE($\hbar\omega$) spectrum of the Cu/*p*-GaN device exhibits a non-monotonic behavior. The IQE gradually increases across the visible spectrum until the interband threshold of Cu is reached at approximately 2.05 eV, at which point a small peak in IQE is clearly observed. After passing the interband threshold of Cu, there is a very slight decline in IQE before a steep increase is observed at higher photon energies ($\hbar\omega > 2.4$ eV) (Figure 2c, solid red curve). This close correlation between the IQE spectral features and the interband threshold of Cu indicates that the

transition from entirely intraband plasmon-assisted excitations to primarily interband excitation exerts a significant influence on the internal device physics of the Cu/*p*-GaN photodiode.

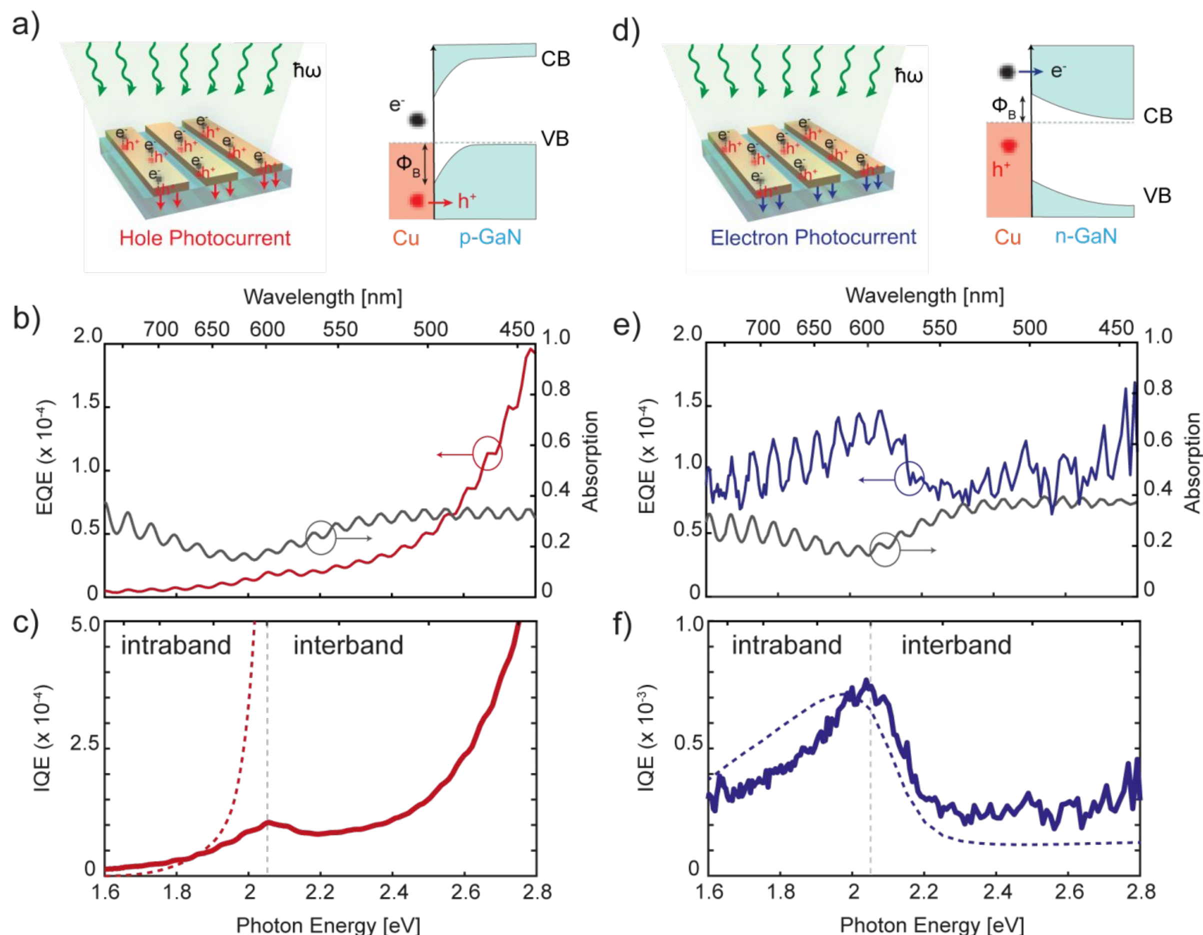

Figure 2: **Photodetection with Plasmonic Cu/GaN Schottky Photodiodes. a)** The Cu/*p*-GaN photodetector geometry and band alignment; **b)** Experimental EQE (red curve) and absorption spectra (grey curve) of the Cu/*p*-GaN photodetector; **c)** Experimental IQE spectrum (solid red curve) of the Cu/*p*-GaN photodetector as a function of incident photon energy along with the theoretically-predicted IQE spectrum (dashed red curve) assuming a simple Fowler model. **d)** The Cu/*n*-GaN photodetector geometry and band alignment; **e)** Experimental EQE (blue curve) and absorption spectra (grey curve) of the Cu/*n*-GaN photodetector; **f)** Experimental IQE spectrum (solid blue curve) of the Cu/*n*-GaN photodetector as a function of incident photon energy along with the theoretically-predicted IQE spectrum (dashed blue curve) assuming a simple Fowler model. The vertical dashed gray line in panels (c) and (f) indicates the interband threshold of the Cu nanoantenna, signifying the transition from entirely intraband excitations to an interband-dominated excitation regime for hot-carrier generation in Cu nanoantennas.

To gain a more complete understanding of hot-carrier energetics at the Cu/GaN interface, we also fabricated similar plasmonic Cu nanoantennas on *n*-type GaN (*n*-GaN) substrates (Figure 2d). Note that this plasmonic Cu/*n*-GaN device operates *via* the collection of hot electrons instead of hot holes, and therefore provides a complementary experimental platform to the Cu/*p*-GaN device. We also emphasize that no interfacial adhesion layer was used at the Cu/*n*-GaN heterojunction, ensuring that the metal/semiconductor interface is identical to the Cu/*p*-GaN device. The interfacial Schottky barrier at the Cu/*n*-GaN heterojunction is around 0.9 eV (Supporting Information Figure S3). Figure 2e shows the absorption spectrum $A(\lambda)$ and the EQE($\hbar\omega$) spectrum from the plasmonic Cu/*n*-GaN photodetector. The EQE($\hbar\omega$) spectrum increases monotonically from 1.6 eV up to a peak around 2 eV, then decreases across a narrow energy range (2 – 2.3 eV), before again increasing at higher photon energies ($\hbar\omega$ > 2.4 eV). We can exclude any contributions from the underlying *n*-GaN support to the observed EQE($\hbar\omega$) spectrum, as no photocurrent was obtained from the bare *n*-GaN substrate in the absence of the Cu nanoantennas (Supporting Information Figure S3). The obtained IQE($\hbar\omega$) spectrum of the Cu/*n*-GaN photodiode (Figure 2f) is very different from that of the Cu/*p*-GaN device that collects hot holes. In particular, Cu/*n*-GaN devices exhibit an abrupt decline in IQE($\hbar\omega$) around 2 eV that remains relatively constant from around 2.2 eV up to 2.8 eV (Figure 2f). To reconcile the significant differences in IQE($\hbar\omega$) between Cu/*p*-GaN (Figure 2c, solid red curve) and Cu/*n*-GaN (Figure 2f, solid blue curve) requires careful analysis of the various electronic processes that determine the IQE($\hbar\omega$) spectrum of hot carrier devices.

1
2
3
4
5
6
7
8
9
10
11
12
13
14
15
16
17
18
19
20
21
22
23
24
25
26
27
28
29
30
31
32
33
34
35
36
37
38
39
40
41
42
43
44
45
46
47
48
49
50
51
52
53
54
55
56
57
58
59
60

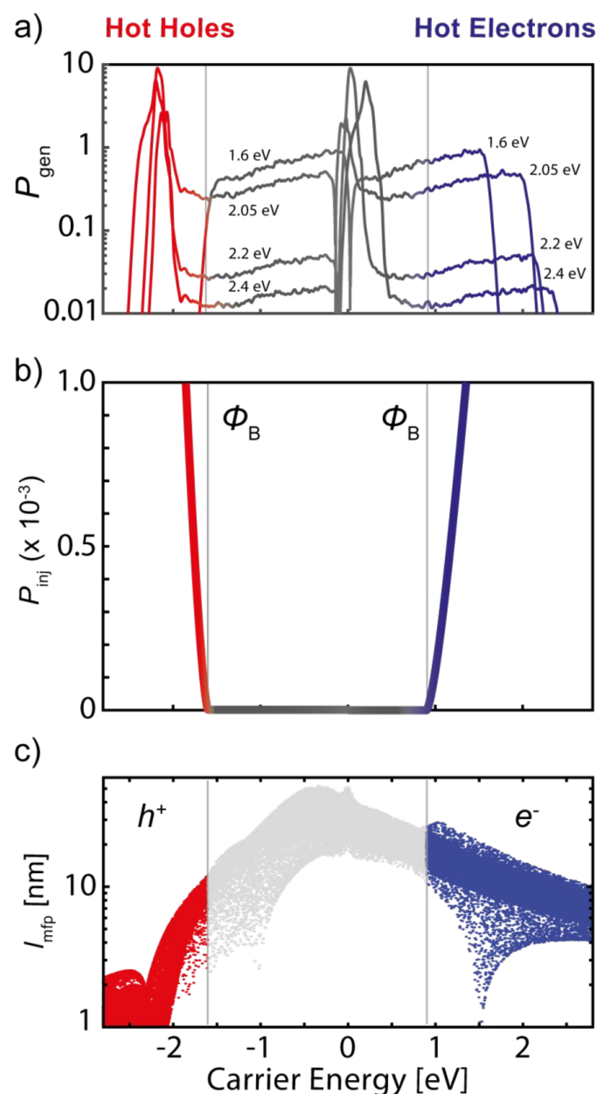

Figure 3: *Ab Initio* Calculations of Hot Carriers in Cu Nanoantennas. **a)** Probability of generating hot carriers (P_{gen}) in Cu at different photon energies below (1.6 eV) and above (2.05 eV, 2.2 eV, 2.4 eV) the interband threshold of Cu. The carrier energies are referenced to the Cu Fermi level located at 0 eV. Negative values of hot-carrier energy correspond to hot holes (left side) and positive values correspond to hot electrons (right side). The vertical gray lines denote the threshold energy (as determined by Schottky barriers, Φ_B) for injection of hot holes and hot electrons across the Cu/p-GaN (Φ_B ~ 1.6 eV) and Cu/n-GaN interface (Φ_B ~ 0.9 eV), respectively. The grey portion of the curves in each panel demarcates the carriers that cannot be collected across the Schottky barrier for either device. The red (blue) portion of the curves shows the fraction of hot holes (hot electrons) that can be collected. **b)** Injection probability (P_{inj}) of hot holes (red) and hot electrons (blue) across the Cu/*p*-GaN and Cu/*n*-GaN interface, respectively, as a function of carrier energy assuming a simple Fowler model employing the parabolic-band approximation. **c)** Mean-free path (l_{mfp}) of hot carriers in Cu as a function of their energy relative to the Cu

1
2
3
4
5
6
7
8
9
10
11
12
13
14
15
16
17
18
19
20
21
22
23
24
25
26
27
28
29
30
31
32
33
34
35
36
37
38
39
40
41
42
43
44
45
46
47
48
49
50
51
52
53
54
55
56
57
58
59
60

Fermi level at 0 eV. Red (blue) portions of the distribution correspond to the fraction of hot holes (electrons) that have sufficient energy to inject across their respective Schottky barriers at the metal/semiconductor interface.

The IQE($\hbar\omega$) of a plasmonic photodetector is determined by both the energy distribution of the generated hot carriers, $P_{\text{gen}}(\varepsilon,\hbar\omega)$, and their injection probability, $P_{\text{inj}}(\varepsilon)$, which accounts for their transport to, and subsequent transfer across, the metal/semiconductor interface, according to the following expression:

$$IQE(\hbar\omega) = \int_{\Phi_B}^{\hbar\omega} P_{\text{gen}}(\varepsilon,\hbar\omega) P_{\text{inj}}(\varepsilon) d\varepsilon \tag{1}$$

where $\hbar\omega$ is the photon energy and ε is the energy of the hot carrier with respect to the metal Fermi level (E_F). Experimentally measuring the IQE($\hbar\omega$) spectrum of a hot-carrier photodetector thus enables the use of theory to unravel the microscopic details governing the behavior of the device.[33] We first analyze the influence of the $P_{\text{gen}}(\varepsilon,\hbar\omega)$ function on the IQE($\hbar\omega$) spectral features observed for the Cu/*p*-GaN and Cu/*n*-GaN devices. Using previously developed *ab initio* methods,[12] we compute the probability of generating hot carriers, $P_{\text{gen}}(\varepsilon,\hbar\omega)$, with a given energy ε relative to the Fermi level ($\varepsilon = E - E_F$) as a function of the incident photon energy $\hbar\omega$ (Figure 3a). Positive values of ε correspond to hot electrons and negative values to hot holes. The colored portion of the curves in Figure 3a denote the subset of hot holes (red) and hot electrons (blue) with energies in excess of their respective Schottky barriers (vertical gray lines) at the Cu/*p*-GaN (Φ_B ~ 1.6 eV) and Cu/*n*-GaN (Φ_B ~ 0.9 eV) interface. In agreement with prior theoretical predictions,[12,34] we observe a dramatic shift in the shape of $P_{\text{gen}}(\varepsilon,\hbar\omega)$ upon crossing the interband threshold of Cu at around 2.1 eV. For purely intraband (*sp*-band to *sp*-band) plasmon-assisted transitions, the energy distributions for both hot electrons and hot holes exhibit nearly uniform probabilities from the Fermi level up to the photon energy. As the photon energy increases, the maximum hot carrier energies increase while the uniform probability decreases (Figure 3a). Above the interband threshold of Cu ($\hbar\omega$ ≥ 2.1 eV), the hot-carrier distributions become highly peaked in probability within a narrow range of energies, consisting of highly-energetic hot holes far below the Cu E_F and hot electrons with much less energy located just above the Cu E_F. Thus, interband transitions in

Cu preferentially generate high-energy hot holes ($\varepsilon \ll 0$) and low-energy hot electrons ($\varepsilon \gtrsim 0$), consistent with prior observations.[20,33,34]

The previous analysis of the $P_{\text{gen}}(\varepsilon,\hbar\omega)$ distribution can partly explain the differences in IQE($\hbar\omega$) spectra for the Cu/*p*-GaN and Cu/*n*-GaN devices, since the onset of interband transitions in the metal exerts opposite effects on the hot hole and hot electron energy distributions relative to the interfacial Schottky barrier. As shown in Figure 3a, the vast majority of hot electrons in Cu/*n*-GaN do not have sufficient energy to overcome the interfacial Schottky barrier for $\hbar\omega$ > 2.1 eV. In contrast, a large proportion of hot holes in the Cu/*p*-GaN device exhibit energies in excess of the Schottky barrier for $\hbar\omega$ > 2.1 eV and should be injected. This analysis of hot-carrier energy distributions relative to the Schottky barrier suggests that the transition from intraband to interband excitations will result in an abrupt drop in IQE($\hbar\omega$) for hot-electron devices and an abrupt increase in IQE($\hbar\omega$) for hot-hole devices. While this prediction is correct for the Cu/*n*-GaN device (Figure 2f), which exhibits a sharp drop in IQE($\hbar\omega$) around 2.1 eV, it is inaccurate for the Cu/*p*-GaN device (Figure 2c). Interestingly, the increase in IQE($\hbar\omega$) for the Cu/*p*-GaN device does not coincide with the onset of the interband dominated regime, but is actually delayed to higher photon energies ($\hbar\omega$ > 2.4 eV). As a result, the observed dip in IQE($\hbar\omega$) spanning from around 2 to 2.3 eV (Figure 2c) cannot be reconciled with an interpretation based solely on the energy distribution of hot holes. To explain the behavior of the Cu/*p*-GaN device therefore requires a closer understanding of the properties of photo-excited hot holes and, in particular, their injection mechanism across the metal/semiconductor interface.

While the $P_{\text{gen}}(\varepsilon,\hbar\omega)$ distribution can be obtained with *ab initio* calculations that accurately account for the metal band structure,[12] the $P_{\text{inj}}(\varepsilon)$ function is typically estimated with a semiclassical Fowler model.[19] This approach is based on a parabolic-band approximation for the electronic structure of both the metal and the semiconductor.[19] The Fowler model also asserts that hot carriers must conserve their energy upon crossing the Schottky barrier, which requires conservation of momentum tangential to the metal/semiconductor interface. These momentum-matching constraints define a narrow escape cone for transmission into the semiconductor, entailing significant reflection losses at the interface. Overall, the Fowler model[3,14,18] predicts an injection efficiency that grows quadratically with respect to the difference between the hot-carrier energy and the Schottky barrier height: $P_{\text{inj}}(\varepsilon) \propto$

1
2
3 $(\varepsilon - \Phi_B)^2$. Since hot carrier mean-free paths (l_{mfp}) are usually commensurate with the nanoscale dimensions of the plasmonic nanoantenna, we initially neglect transport effects. As shown in Figure 3b, $P_{inj}(\varepsilon)$ increases monotonically with hot carrier energy above the Schottky barrier (Φ_B) both for hot electrons (blue portion of the curve) and hot holes (red portion of the curve). Accordingly, we observe that $P_{inj}(\varepsilon)$ rapidly increases beyond 1.6 eV in Cu/*p*-GaN and beyond 0.9 eV in Cu/*n*-GaN (Figure 3b).

Ab initio calculations of electron-electron and electron-phonon scattering[12] were also performed to calculate the mean-free path (l_{mfp}) of hot carriers as a function of energy above (electrons) and below (holes) the Cu Fermi level (Figure 3c). The color scale denotes the fraction of hot holes (red points) and hot electrons (blue points) with energies in excess of their respective Schottky barriers at the metal/semiconductor interface. For both holes and electrons, our calculations predict a decrease in l_{mfp} with increasing carrier energy; note that the l_{mfp} is plotted on a log scale in Figure 3c. Notably, however, there is a substantial asymmetry in l_{mfp} between these hot carriers. For instance, our *ab initio* calculations predict a l_{mfp} of around 1–3 nm for a hot hole 2 eV below the Cu E_F, while a hot electron with similar energy above the Cu E_F exhibits a l_{mfp} of around 8–20 nm (Figure 3c). The much shorter l_{mfp} of hot holes relative to hot electrons suggests that transport effects should be considered for hot-hole-driven devices. Indeed, in the following sections we will show that the energy-dependent l_{mfp} of hot holes exerts a significant influence on the spectral response of the Cu/*p*-GaN photodiode.

Combining the *ab initio*-calculated $P_{gen}(\varepsilon,\hbar\omega)$ distributions with the Fowler $P_{inj}(\varepsilon)$ function described above, we can now evaluate equation 1 to compute the predicted IQE($\hbar\omega$) spectra for each hot carrier device. The result of this calculation for the Cu/*n*-GaN device accurately reproduces both the magnitude and the functional shape of the IQE($\hbar\omega$) spectrum, including the photon energy at which the abrupt decline in IQE($\hbar\omega$) is observed (Figure 2f, blue dashed curve). This near-perfect quantitative agreement between experiment and theory indicates that the parabolic-band approximation intrinsic in the Fowler model is appropriate for modeling hot-electron injection at a metal/semiconductor interface.[3,19] Furthermore, this result demonstrates that it is unnecessary to account for the energy-dependent l_{mfp} of hot electrons to properly describe the behavior of the Cu/*n*-GaN device. In contrast, we observe that this same approach fails to accurately reproduce the salient features of the experimentally-observed IQE($\hbar\omega$) spectrum for the Cu/*p*-GaN photodiode (Figure 2c, red dashed curve).

Such drastic discrepancies between experiment and theory demonstrate that the Fowler model is incapable of explaining the slight decline in IQE($\hbar\omega$) observed beyond the interband threshold of Cu. The inability of the simple $P_{\mathrm{inj}}(\varepsilon)$ function to replicate the IQE($\hbar\omega$) spectrum of the Cu/*p*-GaN device (Figure 2c) indicates that the parabolic-band approximation, along with the failure to account for transport, are both inappropriate simplifications for describing hot holes in the Cu *d*-bands.[32]

To accurately capture the physics of hot-hole injection, we retrieve the unknown $P_{\mathrm{inj}}(\varepsilon)$ function for the Cu/*p*-GaN device by inverting equation (1) and using the experimental IQE($\hbar\omega$) spectrum (Figure 2c) and the *ab initio*-calculated $P_{\mathrm{gen}}(\varepsilon,\hbar\omega)$ function (Figure 3a) as inputs (see Methods). The result of this mathematical procedure is shown in Figure 4a. In the intraband regime ($\hbar\omega$ < 2 eV), a slow Fowler-like rise in $P_{\mathrm{inj}}(\varepsilon)$ is observed with increasing hot-hole energies up to the interband threshold of Cu (ε > –2 eV). We also note that a non-zero injection probability is obtained for carriers with energy lower than the Schottky barrier, which is indicative of tunneling of hot holes across the Cu/*p*-GaN interface (Figure 4a, grey portion of curve). Interestingly, we observe a sharp drop in $P_{\mathrm{inj}}(\varepsilon)$ around the onset of interband transitions at 2.1 eV before the $P_{\mathrm{inj}}(\varepsilon)$ function rises rapidly due to a monotonically growing momentum space for carrier injection (Fowler-like behavior) for very hot holes relative to the Cu Fermi level (ε < –2.4 eV). This feature of the hot-hole injection probability is in stark contrast to the monotonic behavior of $P_{\mathrm{inj}}(\varepsilon)$ for hot electrons (Figure 3b). The discrepancy between the $P_{\mathrm{inj}}(\varepsilon)$ predicted from the Fowler model and that extracted from our mathematical approach indicates that the onset of interband transitions in the metal must trigger an abrupt change of other hot-hole properties, beyond their energy distribution, that strongly impacts their transport to and across the metal/semiconductor interface. Collectively, these results demonstrate that there is a fundamental difference in the origin of the reduction in IQE($\hbar\omega$) observed around the interband threshold of Cu between these two devices (Figure 2c,f). For hot-electron photodetectors (Figure 2f), this feature is associated with a decrease in the $P_{\mathrm{gen}}(\varepsilon,\hbar\omega)$ distribution (Figure 3a, blue portion of curves). In contrast, for hot-hole devices (Figure 2c), the decline in IQE($\hbar\omega$) is related to a drastic decrease of the $P_{\mathrm{inj}}(\varepsilon)$ function (Figure 4a).

1
2
3
4
5
6
7
8
9
10
11
12
13
14
15
16
17
18
19
20
21
22
23
24
25
26
27
28
29
30
31
32
33
34
35
36
37
38
39
40
41
42
43
44
45
46
47
48
49
50
51
52
53
54
55
56
57
58
59
60

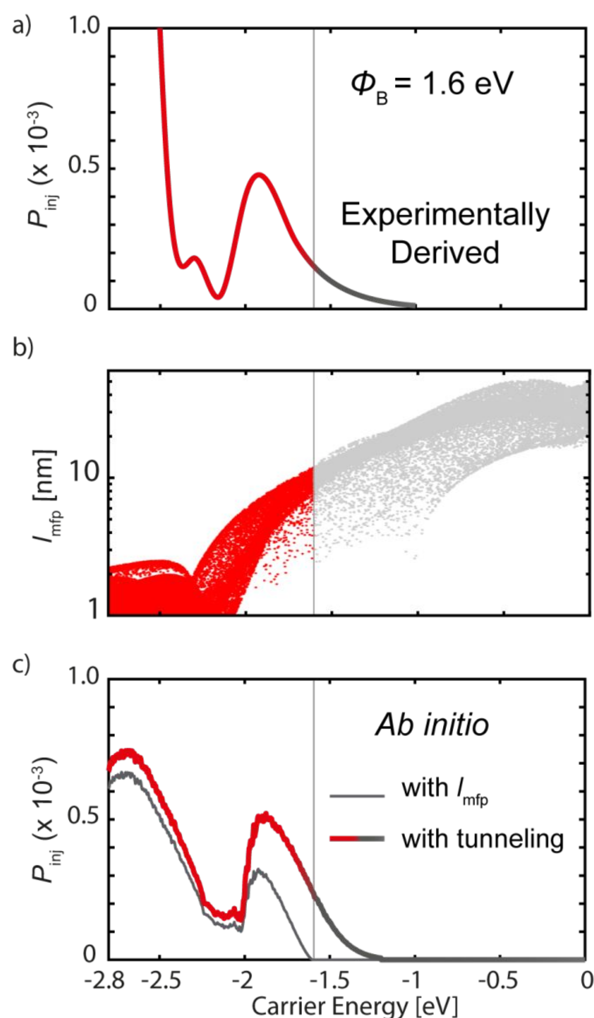

Figure 4: Determination of the Injection Probability (P_{inj}) for Hot Holes at the Cu/p-GaN Interface. **a)** Injection probability for hot holes mathematically extracted from the experimentally-determined IQE spectrum of Cu/*p*-GaN photodetectors. The vertical grey line at 1.6 eV indicates the Schottky barrier height (Φ_B ~ 1.6 eV) at the Cu/*p*-GaN interface. **b)** Mean-free path (l_{mfp}) of hot holes in Cu as a function of their energy relative to the Cu Fermi level at 0 eV. Red portion of the distribution corresponds to the fraction of hot holes that have sufficient energy to inject across the Schottky barrier. **c)** *Ab initio* calculation of the P_{inj} function with various levels of theory. The Fowler model with included transport probability accounting for the energy-dependent mean-free path of hot holes (grey curve), and the full quantum-mechanical model including both the transport and tunneling probabilities (red curve).

We note that the experimentally-derived $P_{\text{inj}}(\varepsilon)$ convolves effects of the transport probability P_{tp} (ε) within the metal and the transmission probability $P_{tm}(\varepsilon)$ across the metal/semiconductor interface (see Methods). *Ab initio* calculations shown in Figure 4b indicate that the mean free path (l_{mfp}) of hot holes generated by interband transitions reduces to just a few nanometers, becoming significantly shorter than the characteristic dimensions (~20–30 nm) of our Cu nanoantennas. Thus, contrary to the case of hot electrons for which transport was neglected, implicitly assuming $P_{tp}(\varepsilon) = 1$, transport effects must be considered for hot-hole devices. We therefore multiply the previously calculated Fowler transmission probability (Figure 3b, red curve) by the transport probability $P_{tp}(\varepsilon)$ that a hot hole reaches the interface while accounting for its energy-dependent l_{mfp} (see Methods). As shown in Figure 4c (grey curve), incorporating this detail introduces a dip in $P_{\text{inj}}(\varepsilon)$ at around 2 eV that is consistent with the experimentally-derived $P_{\text{inj}}(\varepsilon)$ function (Figure 4a). Hence, the non-monotonic behavior of $P_{\text{inj}}(\varepsilon)$ for the hot hole device is attributed to the low carrier velocity and correspondingly short l_{mfp} of *d*-band holes (Figure 4b, red portion of distribution). These results demonstrate that it is critical to account for the limited transport distance of hot holes from the metal *d*-bands when modeling the device physics of a plasmonic photodetector that operates *via* hot-hole collection at photon energies above the interband threshold of the metal nanoantenna.

The incorporation of these transport effects into the device description does not yet explain the significantly non-zero $P_{\text{inj}}(\varepsilon)$ for hot-hole energies below the Schottky barrier (Figure 4a, grey portion of curve). This observation indicates that the Fowler model, which predicts that the responsivity of a hot-carrier photodetector will be zero when the incident photon energy is equal to or below the Schottky barrier height, is incapable of describing this aspect of hot-hole injection at the Cu/*p*-GaN interface. We therefore replace the semiclassical Fowler transport model with a quantum-mechanical model including Fowler-Nordheim tunneling through the Schottky barrier (see Methods). Accounting for the tunneling probability while retaining the transport factor $P_{tp}(\varepsilon)$ discussed above, we find that the obtained $P_{\text{inj}}(\varepsilon)$ function captures both the sub-barrier injection and the reduced probability around the onset of *d*-band transitions (Figure 4c, solid red curve). Treating these various hot-hole effects at the highest level of theory shows excellent agreement with the actual injection probability function extracted from the experimental IQE($\hbar\omega$) measurements (Figure 4a and Supporting Information Figure S4). Therefore, the short l_{mfp} of *d*-band holes at the band onset and the large interfacial fields at the Cu/*p*-GaN interface

1
2
3 necessitate treatment of *both* limited transport distances within the metal nanoantenna and tunneling through the Schottky barrier to explain the measured IQE($\hbar\omega$).

These fundamental differences between the relative energies and velocities of hot electrons and hot holes suggest technological opportunities for employing hot-carrier devices in different frequency regimes. Hot-electron-based photodiodes are expected to exhibit better performance in the near-IR, where the longer l_{mfp} of hot electrons, combined with their greater energy relative to the metal Fermi level, offers significant advantages for enabling efficient injection over an interfacial Schottky barrier. Alternatively, hot-hole-based Schottky junctions are anticipated to offer improved responsivities at higher photon energies (visible to ultraviolet), where the distribution of high-energy hot holes rapidly increases with increasing photon energy. Despite the short transport distances of hot holes at these energies, we note that the IQE from the Cu/*p*-GaN device actually exceeds that of the Cu/*n*-GaN device above 2.7 eV (Supporting Information Figure S5). The response time from both devices is below 10 ms and our observed device responsivities compare favorably to previously reported solid-state plasmonic photodetectors that operate in the visible regime. Indeed, the responsivity from our Cu/*n*-GaN device (~100 nA/mW at 1.8 eV) outperforms our previously reported Au/n-GaN device[33] (~8 nA/mW at 1.8 eV) and exhibits slightly improved performance relative to that observed from Au/TiO_2 (~80 nA/mW at 1.8 eV) and Al/TiO_2 (~40 nA/mW at 1.8 eV) plasmonic photodiodes.[20] Although our studies were not motivated by a desire to create high-performance plasmonic photodiodes, the Cu/*p*-GaN device exhibits a reasonable IQE of 0.5×10^{-3} and a responsivity of around 70 nA/mW at 2.8 eV. Overall, our results suggest that hot-hole-based photodetectors show promise for enabling sensitive plasmonic photodiodes that operate across the visible to ultra-violet regimes.

Conclusion

Through a detailed case-study of Cu-based plasmonic nanoantennas, we have established the critical role of metal band structure on the IQE($\hbar\omega$) spectra of hot-carrier photodetectors that operate *via* the collection of either hot holes (Cu/*p*-GaN) or hot electrons (Cu/*n*-GaN). The interband threshold of the metal nanoantenna determines the spectral profile of the IQE($\hbar\omega$) for a hot-carrier device, but exerts a different effect depending on the sign of the charge carrier that is collected by the underlying

semiconductor. For hot-electron collection, this transition from entirely intraband to primarily interband excitation results in a dramatic drop in device IQE($\hbar\omega$) due to the unfavorable energy distribution of interband hot electrons relative to the metal Fermi level. We note that this behavior is consistent with prior observations on Au-based nanoantennas.[20,34] In contrast, devices that operate *via* hot-hole collection can exhibit favorable IQE($\hbar\omega$) spectra when operating well-beyond the interband threshold of the metal due to the large density of *d*-band states available below the Cu Fermi level. However, we observe that hot-hole transport significantly reduces device performance near the interband threshold of the metal. Overall, the significant difference in hot-carrier l_{mfp} for electrons and holes (Figure 3c) requires careful consideration of the operational regime for these two distinct device polarities along with detailed engineering of interfacial properties (*i.e.* Schottky barrier height and electric near-fields). Our experimental observations strongly indicate that there are considerable advantages associated with building hot-hole photodetectors that function in the ultraviolet to visible regime of the electromagnetic spectrum. Taken together, our experimentally-observed trends supported by first-principles calculations offer general guidelines for the design of hot-carrier-driven devices that operate in the ballistic regime.

Methods

Synthesis and Preparation of Devices

Plasmonic Cu/*p*-GaN photodiodes were constructed onto commercial *p*-type GaN/sapphire substrates (c-axis 0001 orientation) (4 ± 1 µm thick GaN) (Pam-Xiamen). First, a layer of S1813 was spin-coated onto the substrate (40 s, 3000 rpm) and post-baked for 2 min at 115 °C. The Ohmic pattern was exposed for 40 s and then developed for 10 s in MF319®. The sample was then exposed to a mild oxygen plasma (30 s, 200 W, 300 mT) to remove any photoresist residuals. The *p*-GaN substrates were then pre-treated with dilute NH_4OH solution (0.02% v/v%) for 30 s to remove native oxide, followed by 30 s of copious washing in Nanopure water. Consistent with previous observations,[22] it was empirically found that such surface treatments were critical for achieving good device performance. The *p*-GaN/sapphire substrate was then blown dry with N_2 gas and rapidly loaded into the vacuum chamber of an electron-beam evaporator, minimizing exposure to ambient air. Ohmic contacts to the *p*-GaN substrate were fabricated *via* electron-beam physical vapor co-deposition of a 10 nm-thick Ni/Au (50/50 atomic %) alloy followed

1 2 3 4 5 6 7 8 9 10 11 12 13 14 15 16 17 18 19 20 21 22 23 24 25 26 27 28 29 30 31 32 33 34 35 36 37 38 39 40 41 42 43 44 45 46 47 48 49 50 51 52 53 54 55 56 57 58 59 60

by deposition of a 50 nm-thick Au capping layer. After removal of the photoresist in acetone, the sample was annealed in ambient air for 1 h at 500 °C. Subsequently, a layer of PMMA 495-A4 was spin-coated on the sample (1 min, 4000 rpm) and baked for 2 min at 180 °C. Next, a layer of PMMA 950-A2 was spin-coated on top of it (1 min, 5000 rpm) and also baked for 2 min at 180 °C. Then, electron-beam lithography was used to write the nanoantenna pattern (Quanta FEI, NPGS system). Beam currents of approximately 40 pA were used with exposures ranging from 350 $\mu C/cm^2$ to 450 $\mu C/cm^2$, thus achieving different nanoantenna widths with equal pitch. Following PMMA development (15 s in 1:3 MIBK:IPA solution), the same GaN surface preparation procedure was followed (O_2 plasma, NH_4OH etching, DI water rinsing, and N_2 drying). Next, a 25 nm Cu layer was then deposited with electron-beam evaporation (Lesker) (0.8 Å/s, base pressure lower than 2 x 10^{-7} Torr). Using a very thin PMMA photoresist layer and excluding substrate rotation during the electron-beam deposition process, we were able to minimize the lift-off time to just a few minutes. PMMA was thus quickly removed with pure acetone, followed by rinsing in isopropanol and DI water before finally drying with N_2. All measurements were performed within a few hours from the final sample preparation steps to minimize any effects related to surface oxidation in ambient air.

Optical and Electrical Device Measurements

A monochromated laser beam from Fianium supercontinuum laser (2 W) was used as the light source for optical excitation. The beam was collimated and subsequently focused onto the sample with a long working distance, low-NA objective (Mitutoyo 5x, NA = 0.14). The transmitted or reflected power were measured with a Si photodetector. For normalizing the reflection measurements, a silver mirror (M, Thorlabs) was used. Background (BG) was subtracted from all the measurements. In order to continuously monitor the incident laser power, a tilted glass slide was used to deflect a small amount of power from the laser onto a reference photodiode. The incident power was modulated with a chopper, typically at a frequency of ~100 Hz, and the photocurrent signal was subsequently processed with a lock-in amplifier. In order to electrically contact the sample and perform all the photocurrent measurements, piezoelectric micro-probes (Mibots®) are utilized.

Ab Initio Calculations and Theoretical Modelling

Throughout, we use *ab initio* predictions of hot carrier energy distributions $P_{\mathrm{gen}}(\varepsilon,\hbar\omega)$ accounting for direct and phonon-assisted transitions[12] based on density-functional theory and Wannier interpolation for electron-phonon matrix elements as implemented in the JDFTx software.[35] We also compute the lifetimes τ_{kn} and mean-free paths λ_{kn} for each electronic state (specified by wave vector *k* and band *n*) accounting for electron-electron and electron-phonon scattering. See ref. 12 for computational details of the DFT calculations for these quantities.

Determination of the $P_{inj}(\varepsilon)$ function for the hot-hole device is achieved through the following mathematical procedure. Based on the assumption of ballistic collection of hot carriers, we re-write equation (1) from the manuscript as:

$$IQE(\hbar\omega) = IQE_{exp} \sim \int_{\Phi_B}^{hv} P_{inj}(\varepsilon) P_{generation}(\varepsilon,\omega) d\varepsilon$$

We can now use the *ab initio* calculations of $P_{\mathrm{gen}}(\varepsilon,\hbar\omega)$ and the experimental results for $IQE(\hbar\omega)$ to retrieve the value of $P_{inj}(\varepsilon)$ for the hot-hole device. Specifically, we define the following minimization problem:

$$min\left\| IQE_{exp} - \int P_{generation} P_{inj} d\varepsilon \right\|^2$$

Under the constraints: $P_{inj}(\varepsilon) = \begin{cases} > 0 & \varepsilon > \Phi_{\mathrm{B}} \\ = 0 & \varepsilon \leq \Phi_{\mathrm{B}} \end{cases}$

Where : ε,ω: $\Phi_{\mathrm{B}} \rightarrow \omega_{max}$ with ω_{max} being the considered photon energy.

The obtained function $P_{inj}(\varepsilon)$ is shown in Figure 3b of the manuscript and reproduced in Supplementary Information Figure S5.

For analyzing hot carrier transport and injection, we combine key *ab initio* inputs such as the mean-free path λ_{kn} of each electronic state of energy ε_{kn}, with conventional semiconductor modeling techniques relying on a parabolic-band approximation. In particular, our final model for the injection probability, $P_{inj}(\varepsilon) = P_{tp}(\varepsilon) P_{tm}(\varepsilon)$ combines a transport probability $P_{tp}(\varepsilon)$ within the metal and a transmission probability $P_{tm}(\varepsilon)$ across the metal/semiconductor interface. We predict the energy-dependent transport probability according to the following expression:

1
2
3
4
5
6
7
8
9
10
11
12
13
14
15
16
17
18
19
20
21
22
23
24
25
26
27
28
29
30
31
32
33
34
35
36
37
38
39
40
41
42
43
44
45
46
47
48
49
50
51
52
53
54
55
56
57
58
59
60

$$P_{tp}(\varepsilon) = \left\langle \frac{1 - e^{-\left(\frac{d}{L} + \frac{d}{\lambda_{kn}}\right)}}{\left(1 + \frac{L}{\lambda_{kn}}\right)\left(1 - e^{\frac{-d}{L}}\right)} \right\rangle_{\varepsilon_{kn} = \varepsilon}$$

by averaging over all carriers with energy $\varepsilon_{kn} = \varepsilon$ the probability that hot carriers generated with a spatial profile $e^{-z/L}$ reach the interface without scattering based on their individual mean-free paths λ_{kn}. Above, L is the plasmon skin depth, which is approximately 25 nm in the frequency range of interest, and d = 25 nm is the metal film thickness.

We calculate the transmission probability, $P_{tm}(\varepsilon)$, at two levels of theory for comparison. First, we use the Fowler model accounting for both transverse momentum matching and angle-dependent reflection probability.[19] Additionally, we compute the same quantities by explicitly solving Schrödinger's equation within the semiconductor numerically in the presence of an electric field, $\frac{-\nabla^2\psi}{2m^*} + (\varepsilon_F + \Phi_B - Ez)\psi = \psi E$ and matching the value and derivative of ψ to a plane-wave in the metal. In the absence of a field, ψ is a plane-wave in the semiconductor as well, and this reduces exactly to the Fowler model with reflection probability. However, once we solve the Schrödinger equation explicitly with a finite field, we naturally capture tunneling below the barrier (predominantly in the Fowler-Nordheim regime, but we do not make any specific approximations like WKB) and the classical transport above it on the same footing. Specifically, for the calculations shown in Figure 4, we used an electric field of E = 0.7 eV/nm, ε_F = 7.05 eV, and m^* = 0.3 m_e in Cu, and an effective hole mass of m^* = 0.3 m_e in GaN.

Associated Content

The authors declare no competing financial interest.

Supporting Information

Schematic of plasmonic photodiodes, AFM image and absorption spectrum of the Cu/*p*-GaN photodetector, responsivity of bare *p*-GaN, Cu/*p*-GaN, bare *n*-GaN, and Cu/*n*-GaN devices with determination of their respective Schottky barrier heights, direct comparison of IQE spectra for Cu/*p*-GaN and Cu/*n*-GaN devices, and a direct comparison of the experimentally-derived and theoretically-calculated P_{inj} functions for hot-hole injection in Cu/*p*-GaN (PDF). This material is available free of charge *via* the Internet at http://pubs.acs.org.

Corresponding Author

*Email: haa@caltech.edu

ORCID

Giulia Tagliabue: 0000-0003-4587-728X

Joseph S. DuChene: 0000-0002-7145-323X

Ravishankar Sundararaman: 0000-0002-0625-4592

Harry A. Atwater: 0000-0001-9435-0201

Author Contributions

G.T., J.S.D., and H.A.A. conceived of the idea and designed the experiments. G.T. performed all materials synthesis and device characterization. A.H. and R.S. performed all theoretical calculations. G.T. and J.S.D. wrote the manuscript with contributions from all authors. H.A.A. supervised the project. All authors have given approval to the final version of the manuscript.

Acknowledgements

This material is based on work performed by the Joint Center for Artificial Photosynthesis, a DOE Energy Innovation Hub, supported through the Office of Science of the U.S. Department of Energy under Award No. DE-SC0004993. G.T. acknowledges support from the Swiss National Science Foundation through the Advanced Postdoc Mobility Fellowship, grant no. P300P2_171417. A.H. and R.S. acknowledge startup funding from Rensselaer Polytechnic Institute. All theoretical calculations were performed at the Center for Computational Innovations at Rensselaer Polytechnic Institute.

1
2
3
4
5
6
7
8
9
10
11
12
13
14
15
16
17
18
19
20
21
22
23
24
25
26
27
28
29
30
31
32
33
34
35
36
37
38
39
40
41
42
43
44
45
46
47
48
49
50
51
52
53
54
55
56
57
58
59
60

References

(1) Maier, S. A. *Plasmonics: Fundamentals and Applications*; Springer, New York, 2007.

(2) Eustis, S.; A. El-Sayed, M. Why Gold Nanoparticles Are More Precious Than Pretty Gold: Noble Metal Surface Plasmon Resonance and Its Enhancement of the Radiative and Nonradiative Properties of Nanocrystals of Different Shapes. *Chem. Soc. Rev.* **2006**, *35*, 209–217.

(3) Knight, M. W.; Sobhani, H.; Nordlander, P.; Halas, N. J. Photodetection with Active Optical Antennas. *Science* **2011**, *332*, 702–704.

(4) Kelly, K. L.; Coronado, E.; Zhao, L. L.; Schatz, G. C. The Optical Properties of Metal Nanoparticles: The Influence of Size, Shape, and Dielectric Environment. *J. Phys. Chem. B* **2003**, *107*, 668–677.

(5) Barnard, E. S.; Pala, R. A.; Brongersma, M. L. Photocurrent Mapping of Near-Field Optical Antenna Resonances. *Nat. Nanotechnol.* **2011**, *6*, 588–593.

(6) Knight, M. W.; King, N. S.; Liu, L.; Everitt, H. O.; Nordlander, P.; Halas, N. J. Aluminum for Plasmonics. *ACS Nano* **2014**, *8*, 834–840.

(7) Chan, G. H.; Zhao, J.; Hicks, E. M.; Schatz, G. C.; Van Duyne, R. P. Plasmonic Properties of Copper Nanoparticles Fabricated by Nanosphere Lithography. *Nano Lett.* **2007**, *7*, 1947–1952.

(8) Cai, Y.-Y.; Collins, S. S. E.; Gallagher, M. J.; Bhattacharjee, U.; Zhang, R.; Chow, T. H.; Ahmadivand, A.; Ostovar, B.; Al-Zubeidi, A.; Wang, J.; Nordlander, P.; Landes, C. F.; Link, S. Single-Particle Emission Spectroscopy Resolves d-Hole Relaxation in Copper Nanocubes. *ACS Energy Lett.* **2019**, *4*, 2458–2465.

(9) Zia, R.; Schuller, J. A.; Chandran, A.; Brongersma, M. L. Plasmonics: The Next Chip-Scale Technology. *Mater. Today* **2006**, *9*, 20–27.

(10) P. Kuhl, K.; R. Cave, E.; N. Abram, D.; F. Jaramillo, T. New Insights into the Electrochemical Reduction of Carbon Dioxide on Metallic Copper Surfaces. *Energy Environ. Sci.* **2012**, *5*, 7050–7059.

(11) Nitopi, S.; Bertheussen, E.; Scott, S. B.; Liu, X.; Engstfeld, A. K.; Horch, S.; Seger, B.; Stephens, I. E. L.; Chan, K.; Hahn, C.; Nørskov, J. K.; Jaramillo, T. F.; Chorkendorff, I. Progress and Perspectives of Electrochemical CO_2 Reduction on Copper in Aqueous Electrolyte. *Chem. Rev.* **2019**, *119*, 7610–7672.

(12) Brown, A. M.; Sundararaman, R.; Narang, P.; Goddard, W. A.; Atwater, H. A. Nonradiative Plasmon Decay and Hot Carrier Dynamics: Effects of Phonons, Surfaces, and Geometry. *ACS Nano* **2016**, *10*, 957–966.

(13) Narang, P.; Sundararaman, R.; Atwater, H. A. Plasmonic Hot Carrier Dynamics in Solid-State and Chemical Systems for Energy Conversion. *Nanophotonics* **2016**, *5*, 96–111.

(14) Brongersma, M. L.; Halas, N. J.; Nordlander, P. Plasmon-Induced Hot Carrier Science and Technology. *Nat. Nanotechnol.* **2015**, *10*, 25–34.

(15) Tatsuma, T.; Nishi, H.; Ishida, T. Plasmon-Induced Charge Separation: Chemistry and Wide Applications. *Chem. Sci.* **2017**, *8*, 3325–3337.

(16) Christopher, P.; Moskovits, M. Hot Charge Carrier Transmission from Plasmonic Nanostructures. *Annu. Rev. Phys. Chem.* **2017**, *68*, 379–398.

(17) Furube, A.; Du, L.; Hara, K.; Katoh, R.; Tachiya, M. Ultrafast Plasmon-Induced Electron Transfer from Gold Nanodots into TiO_2 Nanoparticles. *J. Am. Chem. Soc.* **2007**, *129*, 14852–14853.

(18) Leenheer, A. J.; Narang, P.; Lewis, N. S.; Atwater, H. A. Solar Energy Conversion *via* Hot Electron Internal Photoemission in Metallic Nanostructures: Efficiency Estimates. *J. Appl. Phys.* **2014**, *115*, 134301.

(19) Chalabi, H.; Schoen, D.; Brongersma, M. L. Hot-Electron Photodetection with a Plasmonic Nanostripe Antenna. *Nano Lett.* **2014**, *14*, 1374–1380.

(20) Zheng, B. Y.; Zhao, H.; Manjavacas, A.; McClain, M.; Nordlander, P.; Halas, N. J. Distinguishing between Plasmon-Induced and Photoexcited Carriers in a Device Geometry. *Nat. Commun.* **2015**, *6*, 1–7.

(21) Chang, L.; Besteiro, L. V.; Sun, J.; Santiago, E. Y.; Gray, S. K.; Wang, Z. M.; Govorov, A. O. Electronic Structure of the Plasmons in Metal Nanocrystals: Fundamental Limitations for the Energy Efficiency of Hot Electron Generation. *ACS Energy Lett.* **2019**, *4*, 2552-2568.

(22) DuChene, J. S.; Tagliabue, G.; Welch, A. J.; Cheng, W.-H.; Atwater, H. A. Hot Hole Collection and Photoelectrochemical CO_2 Reduction with Plasmonic Au/p-GaN Photocathodes. *Nano Lett.* **2018**, *18*, 2545–2550.

(23) Tagliabue, G.; DuChene, J. S.; Abdellah, M.; Habib, A.; Hattori, Y.; Zheng, K.; Canton, S. E.; Gosztola, D. J.; Cheng, W.-H.; Sundararaman, R.; Sa, J.; Atwater, H. A. Ultrafast Studies of Hot-Hole Dynamics in Au/p-GaN Heterostructures, 2018, 1810.04238. *ArXiv. https://arxiv.org/abs/1810.04238* (accessed April 09, 2020).

(24) DuChene, J. S.; Tagliabue, G.; Welch, A. J.; Li, X.; Cheng, W.-H.; Atwater, H. A. Optical Excitation of a Nanoparticle Cu/p-NiO Photocathode Improves Reaction Selectivity for CO_2 Reduction in Aqueous Electrolytes. *Nano Lett.* **2020**, DOI: 10.1021/acs.nanolett.9b04895

(25) Petek, H.; Nagano, H.; Ogawa, S. Hole Decoherence of d-Bands in Copper. *Phys. Rev. Lett.* **1999**, *83*, 832–835.

(26) Alavirad, M.; Olivieri, A.; Roy, L.; Berini, P. High-Responsivity Sub-Bandgap Hot-Hole Plasmonic Schottky Detectors. *Opt. Express* **2016**, *24*, 22544–22554.

(27) Berini, P.; Olivieri, A.; Chen, C. Thin Au Surface Plasmon Waveguide Schottky Detectors on p-Si. *Nanotechnology* **2012**, *23*, 444011.

(28) Goykhman, I.; Desiatov, B.; Khurgin, J.; Shappir, J.; Levy, U. Waveguide Based Compact Silicon Schottky Photodetector with Enhanced Responsivity in the Telecom Spectral Band. *Opt. Express* **2012**, *20*, 28594–28602.

(29) Othman, N.; Berini, P. Nanoscale Schottky Contact Surface Plasmon "Point Detectors" for Optical Beam Scanning Applications. *Appl. Opt.* **2017**, *56*, 3329–3334.

(30) Alavirad, M.; Alavirad, M.; Olivieri, A.; Roy, L.; Berini, P.; Berini, P.; Berini, P. Fabrication of Electrically Contacted Plasmonic Schottky Nanoantennas on Silicon. *Chin. Opt. Lett.* **2018**, *16*, 050007.

(31) Kwon, H.; You, J.-B.; Jin, Y.; Yu, K. Ultra-Compact Silicon Waveguide-Integrated Schottky Photodetectors Using Perfect Absorption from Tapered Metal Nanobrick Arrays. *Opt. Express* **2019**, *27*, 16413–16424.

(32) Sun, Q.; Zhang, C.; Shao, W.; Li, X. Photodetection by Hot Electrons or Hot Holes: A Comparable Study on Physics and Performances. *ACS Omega* **2019**, *4*, 6020–6027.

1
2
3
4
5
6
7
8
9
10
11
12
13
14
15
16
17
18
19
20
21
22
23
24
25
26
27
28
29
30
31
32
33
34
35
36
37
38
39
40
41
42
43
44
45
46
47
48
49
50
51
52
53
54
55
56
57
58
59
60

(33) Tagliabue, G.; Jermyn, A. S.; Sundararaman, R.; Welch, A. J.; DuChene, J. S.; Pala, R.; Davoyan, A. R.; Narang, P.; Atwater, H. A. Quantifying the Role of Surface Plasmon Excitation and Hot Carrier Transport in Plasmonic Devices. *Nat. Commun.* **2018**, *9*, 3394.
(34) Sundararaman, R.; Narang, P.; Jermyn, A. S.; Iii, W. A. G.; Atwater, H. A. Theoretical Predictions for Hot-Carrier Generation from Surface Plasmon Decay. *Nat. Commun.* **2014**, *5*, 5788.
(35) Sundararaman, R.; Letchworth-Weaver, K.; Schwarz, K. A.; Gunceler, D.; Ozhabes, Y.; Arias, T. A. JDFTx: Software for Joint Density-Functional Theory. *SoftwareX* **2017**, *6*, 278–284

TOC Image